Composite Structures 189 (2018) 366–377

Contents lists available at ScienceDirect

Composite Structures

journal homepage: www.elsevier.com/locate/compstruct

Comparison of stress-based failure criteria for prediction of curing induced damage in 3D woven composites

Borys Drach[a,*], Igor Tsukrov[b], Anton Trofimov[c], Todd Gross[b], Andrew Drach[d]

[a] Mechanical & Aerospace Engineering, New Mexico State University, Las Cruces, NM, USA
[b] Mechanical Engineering, University of New Hampshire, Durham, NH, USA
[c] Center for Design, Manufacturing and Materials, Skolkovo Institute of Science and Technology, Skolkovo, Russia
[d] Institute for Computational Engineering & Sciences, University of Texas at Austin, Austin, TX, USA

ARTICLE INFO

Keywords:
3D woven composites
Mesoscale
Finite element analysis
Failure criteria
Microcracking
Damage
Curing

ABSTRACT

Several stress-based failure criteria (von Mises, dilatational strain energy density, parabolic stress and Drucker-Prager) are implemented in a numerical model of a 3D woven composite to predict initiation of damage due to cooling after curing. It is assumed that the composite is completely cured at elevated temperature and the residual stresses arise due to difference in the thermal expansion coefficients of fibers and matrix. The stresses are found by finite element analysis on the mesoscale while the effective thermoelastic properties of fiber tows are determined by micromechanical modeling. The matrix is modeled as an isotropic material with temperature dependent elastic properties and thermal expansion coefficient.

Comparison of numerical simulation results with the microcomputed tomography data obtained for a one-by-one orthogonally reinforced carbon/epoxy composite shows that the parabolic stress and the dilatational strain energy criteria provide the most accurate predictions of cure-induced damage. However, the accuracy of the parabolic failure criterion is dependent on the choice of the mechanical tests used to determine the values of its two material parameters.

1. Introduction

3D woven composites are a relatively new class of materials possessing superior mechanical properties compared to 2D woven composite laminates. This advantage comes from continuous reinforcement in all three dimensions resulting in high strength and additional fatigue resistance of the 3D woven composites under multiaxial loading. The reinforcement architecture can be designed for specific applications [1]. As such, parts manufactured as 3D woven composites have been increasingly used in aerospace industry and other performance-driven applications such as those in the automotive or power industries.

Some 3D woven composite material systems, however, are prone to matrix microcracking during manufacturing. Fig. 1 illustrates microcracks that developed in a 3D woven carbon/epoxy composite with significant through-thickness reinforcement after matrix curing at elevated temperature. We assume that the major factor in processing-induced microcracking of woven composites is the residual stress due to mismatch of thermal expansion coefficients (CTEs) of carbon fibers and epoxy matrix developing when completely cured matrix cools from the curing to room temperature. Note that other contributing factors to the development of the residual stress may include flow- and thermal-induced stresses during resin injection and chemical shrinkage due to cure [2,3].

The residual stresses resulting from the elevated temperature curing of composites with thermoset matrices have been investigated in several publications. On the microscale (interaction between fibers), Jin et al. [4] studied the effect of fiber arrangement, i.e. square, hexagonal and random, on the distributions of residual thermal stresses in carbon fiber reinforced polymers (CFRPs). Zhao et al. [5], and Yang et al. [6] studied the effect of residual stresses due to cooling after curing on the strength of unidirectional glass-fiber reinforced composites using 2D FEA with maximum normal stress and Drucker-Prager failure criteria, respectively. Lu et al. [7] and Han et al. [8] performed similar studies for carbon fiber reinforced polymers using 3D FEA with, correspondingly, parabolic and Drucker-Prager failure criteria. Karami et al. [9] and Han et al. [10] employed 3D FEA to evaluate residual stresses in the matrix around fibers of bidirectional composites. On the mesoscale (interaction between yarns or tows), Sweeting and Thomson [11] used FEA to examine maximum principal stress distribution in Z-pinned laminated composite structures. The authors concluded that the stresses in the matrix around Z-pins exceeded failure stresses and therefore microcracking was to be expected. Their conclusions were supported by

* Corresponding author at: Mechanical and Aerospace Engineering, New Mexico State University, P.O. Box 30001, MSC 3450, Las Cruces, NM 88003-8001, USA.
E-mail address: borys@nmsu.edu (B. Drach).

https://doi.org/10.1016/j.compstruct.2018.01.057
Received 15 April 2017; Received in revised form 6 January 2018; Accepted 19 January 2018
0263-8223/

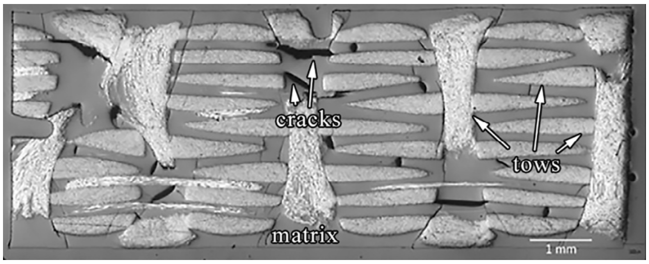

Fig. 1. Optical micrograph of a 3D woven composite with significant through-thickness reinforcement showing microcracking in the matrix.

the microscopy data. Xiong et al. [12] proposed a micromechanical model for prediction of residual thermal stresses in plain-weave fabric composites. On the macroscale, Hirsekorn et al. [13] simulated warpage of a homogenized asymmetric composite laminate after curing and compared the results with experimental measurements.

A comprehensive study involving thermo-mechanical tests of the neat resin was presented in a series of papers [14–16]. The authors utilized experimental data to establish the material parameters of the resin and predicted possible matrix failure assuming fully cured resin and using either the equivalent von Mises stress or the so-called "parabolic" failure criterion (see discussion in Section 3 of this paper). Systematic characterization of RTM6 epoxy resin was performed in [17] including its chemically induced volumetric shrinkage during curing, temperature dependence of its Young's modulus and CTE, and the resin's relaxation behavior for different temperatures and degrees of cure. The numerical simulations in the paper were limited to unidirectional carbon epoxy composites with square packing of fibers.

It is well known that thermoset resins exhibit time dependent viscoelastic behavior. These effects are more pronounced in the viscous liquid state prior gelation and rubbery solid state between gelation and vitrification [18]. Comprehensive numerical modeling of these effects has been discussed in [18–20]. The authors concluded that the full viscoelastic formulation can be substituted by path dependent constitutive model that incorporates the temperature dependent stiffness of resin [20]. Several papers addressed the issue of chemical shrinkage and its contribution to the residual stresses after curing. According to [21], most of the curing shrinkage in RTM6 resin occurs before vitrification when the elastic shear modulus of the resin is too low to generate significant residual stresses. This was also confirmed by our measurements of the development of stresses during constrained cooling after curing as reported in [22]. Such a treatment is in good agreement with the parametric studies in [17] and the approach presented in [23] where the authors state, based on their experimental work, that for carbon fiber reinforced RTM6 composites contribution from the chemical shrinkage of the RTM6 matrix can be omitted.

The primary objective of this paper is to present a numerical modeling approach to quantifying processing-induced residual stresses in 3D woven composites with significant through-thickness constraint and predict initiation of damage in their resin rich areas. We validate our model predictions by comparing the simulation results with available X-ray computed microtomography data. For this purpose, we develop realistic finite element models of the composite on mesoscale, and perform numerical simulations utilizing micromechanically homogenized properties of resin infiltrated carbon tows and temperature-dependent material properties of resin. Our main assumption is that residual stresses arise solely from the difference in CTEs between carbon fibers and epoxy matrix during cooling from the curing to room temperature and that, as discussed above, the chemical shrinkage and viscoelastic effects can be ignored.

The paper is organized as follows. Section 2 describes our approach to geometric modeling and generation of finite element mesh of a 3D woven composite unit cell. The four stress-based failure criteria considered for damage initiation predictions are introduced in Section 3. Section 4 presents the temperature dependent material properties of the matrix and the micromechanical homogenization formulas used to predict the effective thermo-elastic properties of the reinforcement tows. The results of the finite element analysis are given in Section 5. They include calculation of the effective elastic properties of the composite at room temperature and distribution of residual stresses due to cooling after curing. In the same section, we compare the processing-induced damage initiation predictions of the four stress-based criteria with the X-ray computed microtomography observations performed on actual composite specimens. Section 6 presents the conclusions of this research.

2. Finite element mesh preparation

Thermal mismatch stresses in 3D woven composites can be quantified by utilizing numerical models on the meso-scale (see other studies on meso-scale, e.g. [24–26]). In these models the composite is represented as a two-phase material consisting of homogenized bundles of fibers (tows) and a matrix, as illustrated in Fig. 2. The tows are classified as warp (longitudinal), weft (transverse) and binder (through-thickness) based on their directions. The configuration shown in Fig. 2 is the so-called "one-to-one orthogonal" reinforcement architecture that has possibly the maximum through-the-thickness constraint of 3D woven architectures. Note that at the micro-scale, tows consist of several thousands of individual fibers. An accurate prediction of the intra-tow damage initiation and the resulting tow failure would require multiscale modeling including both meso- and micro-scales. However, for the purpose of studying the cure-induced microcracking of matrix, we restrict ourselves to the dual-phase meso-scale model utilizing independently homogenized properties of tows.

The meso-scale FEA models of woven composites are usually developed for the smallest repeating portion of the material – the so-called "unit cell" (UC). The entire composite is represented as a continuous assemblage of such unit cells. We use the numerically simulated geometry of woven reinforcement for unit cells [27,28] to develop three-

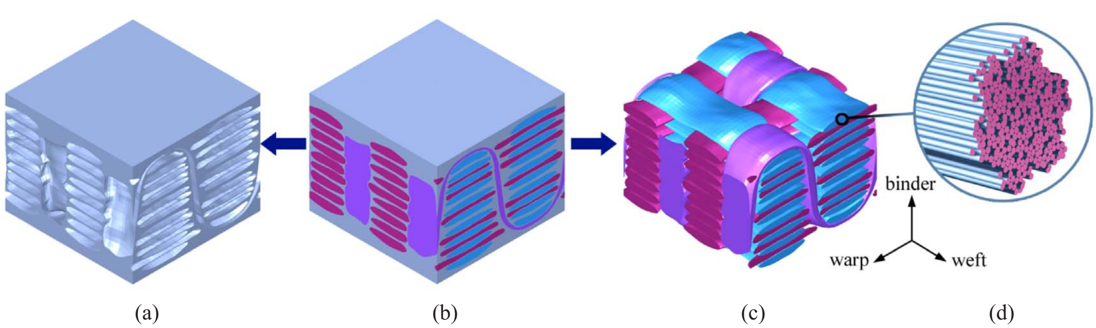

Fig. 2. The structure of 3D woven composite material on meso- and micro- scales: a) matrix; b) composite unit cell; c) reinforcement represented by bundles of carbon fibers (tows); d) individual filaments in a tow.

dimensional finite element models of the considered composites as described in [29]. These models are subjected to the appropriate loading and boundary conditions to determine distributions of stresses in the matrix and tows. Periodic boundary conditions are prescribed to the corresponding faces of the UC to preserve periodicity of the UC and material continuity. An overview of the model development and implementation is given below.

Numerical modeling of three-dimensional woven composites presents significant challenges related to accurately representing the as-woven geometry of the reinforcement. The approaches found in the literature are either based on the nominal description of composites or involve a certain degree of mechanically justified deformation of the tows. The most commonly used software packages are TexGen, WiseTex, DYNAFAB, ScotWeave, DFMA, and LS-Dyna as described, for example, in [27,30–33].

In this paper we consider an example of the one-to-one orthogonally reinforced composite panel consisting of ten layers of warp and weft tows with a through-thickness binder tow as can be seen, for example, in Fig. 1. The panel is 4.1 mm thick with in-plane unit cell dimensions of 5.1 × 5.1 mm. The finite element (FE) mesh of the unit cell is generated based on the results of fabric mechanics simulations performed in DFMA software (see [27,34,35] and later publications by the research group). In the simulations, the user starts with generating an initial pattern of the reinforcement architecture based on the weave pattern, number of tows, their areas and intertow spacing. The tows in the initial pattern (represented by single a cylindrical fiber each) are then subdivided into sub-tows subjected to tensile forces. The relaxation of these forces mimics the weaving process of 3D woven composites. For better accuracy, the number of sub-tows is increased and the relaxation process is repeated until a realistic reinforcement geometry is achieved.

One of the challenges in the conversion of the geometrical model into a robust FE mesh is the commonly occurring geometric incompatibility problem, which is manifested in the interpenetration of tow cross-sections. Several authors [36–38] have developed remedial procedures including semi-automatic deformations of the tow shapes, reductions of their cross-sectional area, and special procedures to prescribe changes in cross-sectional area and/or axial rotation of tows. We developed a MATLAB script to automatically process the reinforcement surface mesh exported from DFMA and remove geometric incompatibilities. The script identifies the nodes of a tow inside another tow and moves them in the direction of the mean normal of all penetrating surface elements until interpenetration is removed. This method ensures minimal disturbance of the tow geometry and produces FEA mesh of the reinforcement geometry ready for analysis. Fig. 3 illustrates our geometric model development and its comparison with X-ray computed microtomography scan. Good correlation between the generated and the actual microstructures is observed.

The FE mesh of the UC (see Fig. 4) is imported into the commercial FEA software MSC Marc Mentat. The reinforcement and matrix meshes are processed as separate element sets. All model preparation steps are performed automatically within the MSC Mentat software using a custom Python script. At the completion of script, the user is presented with a ready-to-run model. The use of the automation script not only streamlines the process of model preparation, but also ensures consistency of the simulation results data. This, in turn, simplifies post-processing of the data from various loadcases and architectures. The details of DFMA output processing and FEA model preparation can be found in [29,39].

3. Damage initiation criteria

There are several possible mechanisms of failure of glassy polymers that can be activated by different states of stress in the material. They are reflected in various failure criteria used to predict initiation of damage in the polymer using the components of stress tensor.

The most popular criterion is based on the second invariant of the stress tensor (von Mises yield criterion) and assumes that the resin failure is accommodated by deviatoric yielding. The criterion has been applied, for example, in [16] to investigate microscopic yielding of epoxy matrix in unidirectional carbon fiber composites due to the residual stressed caused by cooling the composites from curing to room temperature. However, this approach does not predict failure when polymers are subjected to stresses with a substantial dilatational (hydrostatic tension) component. In such cases, the first invariant of the stress tensor has to be included, as discussed, for example, in [40,41]. The authors refer to these types of criteria as pressure-modified von Mises criteria. In the cases when the deviatoric component of stress is considerably lower than what is required for shear yielding so that the dilatational effects are dominant, [40] propose to use the dilatational energy criterion, see also [23] and [42].

In this paper, we compare the ability of the above mentioned approaches to predict initiation of damage in the matrix of a 3D woven carbon/epoxy composite as it cools down from the curing to room temperature, which causes residual stresses due to the mismatch of the CTEs between the carbon fibers and epoxy matrix. Note that several research groups proposed to apply separate failure conditions to different states of stress in the matrix [43,44]. However, we focus on whether a single criterion can be universally applied to all complex stress states and satisfactory predict initiation of cure-induced damage in the matrix of a 3D woven composite.

The following criteria are investigated.

1. **Von Mises criterion** was originally proposed to predict yielding in metals, but was subsequently applied to ductile failure of other classes of materials [45]. According to this criterion, the material will not yield if the equivalent stress calculated as $\sigma_{VM} = \sqrt{0.5[(\sigma_1 - \sigma_2)^2 + (\sigma_1 - \sigma_3)^2 + (\sigma_2 - \sigma_3)^2]}$ is below the critical value:

$$\sigma_{VM} \leqslant \sigma_{VM}^{crit} \tag{1}$$

where σ_1, σ_2, σ_3 are the principal stresses. In our simulations, we use the critical value $\sigma_{VM}^{crit} = 67.8\,MPa$ chosen based on the fracture stress measurements reported in [17].

2. **Dilatational energy criterion** is based on the energy required for crack initiation by void nucleation. The criterion was originally utilized for triaxial state of stress in glassy polymers in [40], where the stress energy density is calculated assuming linear material behavior

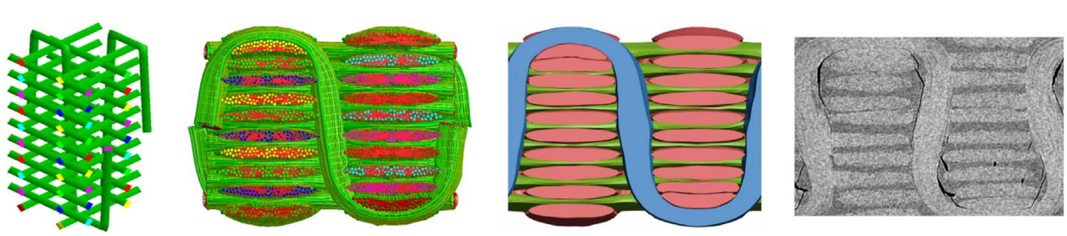

(a) (b) (c) (d)

Fig. 3. Our geometric modeling approach: (a) weave pattern; (b) result of the fabric mechanics simulation; (c) meshed tows after elimination of geometric incompatibilities; (d) microtomography image of actual composite.

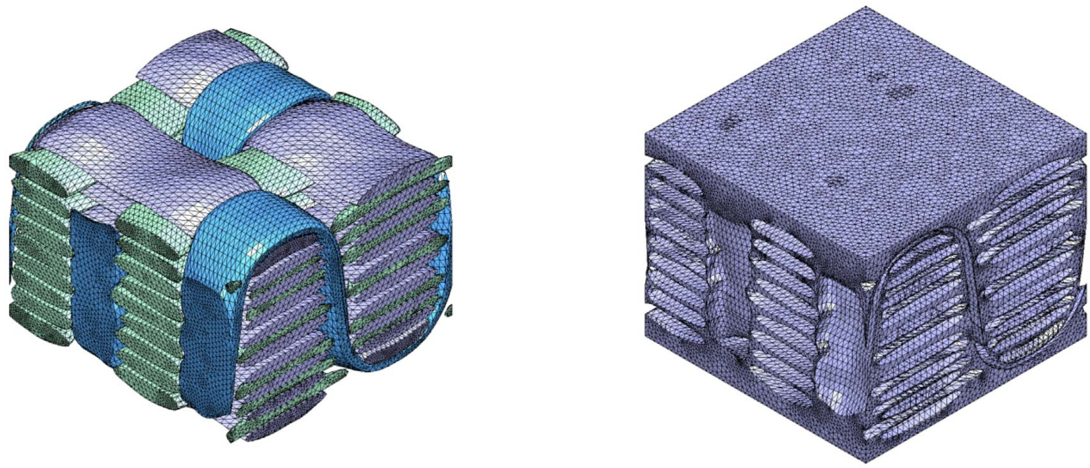

(a) (b)

Fig. 4. Final FE surface mesh of the (a) one-to-one orthogonal reinforcement and (b) matrix.

$$U_\nu = \frac{1-2\nu}{6E}(\sigma_1 + \sigma_2 + \sigma_3)^2 \tag{2}$$

where E is the Young's modulus and ν is the Poisson's ratio of the material. This criterion can be re-written as

$$\sigma_H \leqslant \sigma_H^{crit}, \tag{3}$$

where $\sigma_H = \frac{1}{3}(\sigma_1 + \sigma_2 + \sigma_3)$ is the hydrostatic stress, and σ_H^{crit} is the value of hydrostatic stress that corresponds to the critical energy density required for cavitation. The approaches to determine this value include the poker chip experiments [41,46,47], the constrained tube method [22,48] and evaluation of σ_H^{crit} from uniaxial tensile tests [22]. We use the value $\sigma_H^{crit} = 58.7\,MPa$ based on the estimate of $U_\nu^{crit} = 0.4\,MPa$ for RTM6 epoxy provided in [23].

3. **Parabolic failure criterion** was utilized in [15] based on the description provided in [40]. It combines the first and the second invariants of stress as

$$\sigma_{VM}^2 + A\sigma_H \leqslant B^{crit} \tag{4}$$

The material parameters A and B^{crit} are found from mechanical testing of the material.

For RTM6, two sets of values for A and B^{crit} can be produced based on the test results reported in the literature. Asp et al. [23] provide failure stresses for RTM6 in tension and compression as $\sigma_{yt} = 82\,MPa$ and $\sigma_{yc} = 134\,MPa$. Using formulae (3), (4) from [40] (see also [49]) we obtain $A = 156\,MPa$, $B^{crit} = 10{,}990\,(MPa)^2$. Hobbiebrunken et al. [15] evaluate these parameters based on uniaxial tension and torsion tests. In our notation, their results correspond to $A = 339\,MPa$, $B^{crit} = 17{,}370\,(MPa)^2$. Both of these sets of values are considered in this paper.

4. **Bauwens** (Drucker-Prager) criterion assumes that the linear combination of von Mises and hydrostatic stress are utilized to predict failure [40]:

$$\sigma_{VM} + C\sigma_H \leqslant D^{crit} \tag{5}$$

The material constants C and D^{crit} can be evaluated from the results of two mechanical tests, e.g. tension and compression or torsion and biaxial tension. In this paper, based on tension and compression results $\sigma_{yt} = 82\,MPa$ and $\sigma_{yc} = 134\,MPa$ provided in [23], the material parameters are chosen as $C = 0.722$, $D^{crit} = 50.9\,MPa$.

Note that the dilatational energy density, parabolic and Bauwens criteria predict different critical values for the hydrostatic stress in the absence of the deviatoric stresses. When σ_{VM} is equal to zero, failure is predicted at $\sigma_H = 58.7, 70.5, 51.2, 70.5\,MPa$ by the dilatational energy density, the parabolic criterion with the material parameters based on [23], the parabolic criterion with the material parameters based on [15] and the Bauwens criterion, respectively. This difference is defined by two factors – the choice of the criterion and the choice of the experiments used to determine the numerical coefficients in the criterion. The disparity between the criteria is even more noticeable when we compare the predictions of the critical von Mises stresses in the absence of the hydrostatic component: $\sigma_{VM} = 67.8, 104.8, 131.8, 50.9\,MPa$ for the von Mises, the parabolic criterion with the material parameters based on [23], the parabolic criterion with the material parameters based on [15] and the Bauwens criterion, respectively.

Given that different mechanical tests result in different critical values of σ_{VM} and σ_H, one might speculate that the failure criterion at a given point has to be chosen based on the local state of stress rather than using the same criterion for the entire volume of the material. However, in this paper, we investigate whether a single universal criterion (one of the four presented above) can be successfully used to predict damage initiation in the matrix of a 3D woven composite during cooling after curing.

4. Material properties of the constituents

4.1. Temperature dependent thermo-mechanical behavior of the matrix material

The matrix phase (fully cured HEXCEL RTM6 epoxy resin) is simulated as a linear isotropic material with constant Poisson's ratio $\nu_m = 0.35$, and temperature dependent Young's modulus and thermal expansion coefficient [17]:

$$E_m = E_m^{0^\circ C} - \beta_m T \tag{6}$$

$$\alpha_m = \alpha_m^{0^\circ C} + \gamma_m T \tag{7}$$

where $E_m^0 = 3500\,MPa$, $\beta_m = 5.9\frac{MPa}{^\circ C}$, $\alpha_m^{0^\circ C} = 5\cdot 10^{-5}\frac{1}{K}$, $\gamma_m = 1.0510^{-7}\frac{1}{K\cdot{}^\circ C}$ are the material parameters, and T is the temperature in °C.

4.2. Homogenized thermo-elastic properties of the tows

In our models, the resin-impregnated fiber tows are modeled as homogenized transversely isotropic solids. It is assumed that unidirectional continuous filaments are randomly distributed in the isotropic matrix within the tows. There are several micromechanical formulas available to predict the effective thermo-elastic parameters of such material systems. One of the popular approaches in the woven composites literature is to use the formulas proposed in [50], see [37]. However, such predictions might not satisfy the energetically rigorous Hashin-Strikman bounds [51], see [52,53]. We utilized the following formulas based on [54,55] to predict the effective thermal expansion coefficients and elastic moduli of the resin-impregnated unidirectional fibers [56]:

$$\alpha_{1t} = \frac{E_{1f}\alpha_{1f}V_f + E_m\alpha_m V_m}{E_{1f}V_f + E_m V_m}, \tag{8}$$

$$\alpha_{2t} = \alpha_{2f}V_f\left(1 + \nu_{12f}\frac{\alpha_{1f}}{\alpha_{2f}}\right) + \alpha_m V_m(1 + \nu_m) - (\nu_{12f}V_f + \nu_m V_m)\alpha_{1t}, \tag{9}$$

$$E_{1t} = V_f E_{1f} + V_m E_m + \frac{4(\nu_{12f}-\nu_m)^2 V_f V_m}{V_m/k_f + V_f/k_m + 1/G_m}, \tag{10}$$

$$\nu_{12t} = V_f\nu_{12f} + V_m\nu_m + \frac{(\nu_{12f}-\nu_m)(1/k_m - 1/k_f)V_f V_m}{V_m/k_f + V_f/k_m + 1/G_m}, \tag{11}$$

$$G_{12t} = G_m + \frac{V_f}{\frac{1}{G_{12f}-G_m} + \frac{V_m}{2G_m}}, \tag{12}$$

$$E_{2t} = \frac{4k^*G_{23t}}{k^* + n\cdot G_{23t}}, \tag{13}$$

$$\nu_{23t} = \frac{k^* - n\cdot G_{23t}}{k^* + n\cdot G_{23t}}, \tag{14}$$

where $k_f = \left(\frac{4}{E_{2f}} - \frac{1}{G_{23f}} - \frac{4\cdot\nu_{12f}^2}{E_{1f}}\right)^{-1}$, $k_m = \left(\frac{4}{E_m} - \frac{1}{G_m} - \frac{4\cdot\nu_m^2}{E_m}\right)^{-1}$, $k^* = k_m + V_f\frac{(k_f-k_m)(k_m+G_m)}{k_m+G_m+V_m(k_f-k_m)}$, $n = 1 + \frac{4k^*\nu_{12t}^2}{E_{1t}}$, $G_{23t} = G_m\left[1 + \frac{(1+\beta_1)V_f}{\rho - V_f\left(1 + \frac{3\beta_1^2V_m^2}{\eta\cdot V_f^3+1}\right)}\right]$

and $\gamma = \frac{G_{23f}}{G_m}$, $\eta = \frac{\beta_1 - \gamma\cdot\beta_2}{1+\gamma\cdot\beta_2}$, $\rho = \frac{\gamma+\beta_1}{\gamma-1}$, $\beta_1 = \frac{k_m}{k_m+2G_m}$, $\beta_2 = \frac{k_f}{k_f+2G_{23f}}$.

Constants E, G, ν, α are the Young's moduli, shear moduli, Poisson's ratios and thermal expansion coefficients, correspondingly; direction 1 is longitudinal (tow direction), and directions 2 and 3 are transverse; subscript "f" refers to "fibers" and subscript "m" refers to "matrix".

The tows consist of 12,000 IM7 carbon fibers impregnated with RTM6 epoxy. The volume fraction of fibers within the tows is set to 80%. Based on the fiber properties provided in Table 1 and the resin properties $E_m = 2.89\ GPa$, $\nu_m = 0.35$, $\alpha_m = 65\cdot10^{-6}\frac{1}{K}$ given in Table 2 of [17], the following properties of the tow are obtained: $E_{1t} = 221.38\ GPa$, $E_{2t} = 13.18\ GPa$, $G_{12t} = 7.17\ GPa$, $\nu_{12t} = 0.35$, $\nu_{23t} = 0.35$, $\alpha_{1t} = -2.29\cdot10^{-7}\frac{1}{K}$, $\alpha_{2t} = 2.23\cdot10^{-5}\frac{1}{K}$. Note that the properties of the matrix in the tows change with temperature, see formulas 6 and 7. However, these changes will result in insignificant variations of the homogenized properties of the tows (see comparison in Table 2), so in the numerical simulations the properties of the tows are assumed to be temperature independent.

The material orientations (principal material axes in the finite elements relative to the global coordinate system of the FE mesh) of the tows are assigned using the data from DFMA simulations as described in [29]. The major principal axis for each of the tow elements is aligned with the tow centerline (Fig. 5). The second principal axis is taken in radial direction from the centerline to FE centroid. The third principal direction is defined as the vector product of the first two.

5. Numerical simulations

Two types of analysis are presented in this work: (1) mechanical loading at room temperature to evaluate effective elastic properties of the composite; and (2) cooling after resin curing. Both analysis types involve application of periodic boundary conditions as described below.

5.1. Periodic boundary conditions and effective elastic properties

In our meso-scale numerical modeling, we employ periodic boundary conditions prescribed on the external lateral surfaces of the composite UC to preserve the material continuity on the macroscale (see, for example, [29,57–59]). The considered unit cell represents the total thickness of the composite, therefore, periodic boundary conditions in the thickness direction are not prescribed. The boundary conditions in displacements are formulated in [60] as:

$$u_i^+ = u_i^- + \delta_i \ (i = warp,\ weft) \tag{15}$$

where u_i^+ and u_i^- are the components of the corresponding nodal displacements on the positive and negative faces; δ_i is the average displacement.

Conditions (15) are implemented in MSC Marc/Mentat using its "servo-link" feature [42,61]. Servo-links are used to prescribe multipoint boundary conditions for nodal displacements in the form of a linear function with constant coefficients. In such an implementation, δ_i represent translational degrees of freedom of a free (control) node, to which nodes on the opposite faces of the UC are linked. The approach requires congruent meshes on the lateral surfaces of the UC, which is ensured by our meshing procedure, see Section 2.

To determine the effective elastic properties of the unit cell shown in Fig. 4 we subject the UC to 6 load cases: 3 uniaxial tension and 3 shear cases. In our notation, x-axis is the warp direction, y-axis is the weft direction and z-axis is the through-thickness direction. The boundary conditions for each load case are applied to the control nodes (see above) in terms of displacements that correspond to the prescribed values of macroscopic strain ε^0. The results of the numerical simulations are processed using a custom Python script to extract volume-averaged stress values as follows:

$$\langle\sigma_{ij}\rangle_m = \frac{1}{V}\sum_{l=1}^{N_e}(\sigma_{ij}^{(l)})_m\cdot V^{(l)}, \quad i,j = 1,2,3 \tag{16}$$

where $\langle\sigma_{ij}\rangle_m$ is the volume average of the stress component ij calculated from the m-th loadcase, V is the UC volume, $(\sigma_{ij}^{(l)})_m$ is the stress component ij at the centroid of the finite element l calculated from the m-th loadcase, $V^{(l)}$ is the volume of the element l, and N_e is the total number of elements in the model.

The overall material stiffness components C_{ijkl}^{eff} are defined as the proportionality coefficients relating macroscopic strains with volume-averaged stresses:

$$C_{ijkl}^{eff}\cdot\varepsilon_{kl}^0 = \langle\sigma_{ij}\rangle, \quad i,\ j,\ k,\ l = 1,2,3 \tag{17}$$

where the summation over the repeating indices is assumed. The orthotropic engineering constants of the composite were found from C_{ijkl}^{eff} and are reported in Table 3 for the considered UC. These values are in good correspondence with the experimental results obtained via standard tensile tests with digital image correlation strain measurement as described in [62].

The value of ν_{xy} presented in Table 3 appears unusually low and deserves an explanation. We believe that this specific value of the Poisson's ratio represents the result of two competing mechanisms. In a homogeneous material, simple tension along x-axis is accompanied by contraction along y and z axes equal to the tensile strain multiplied by

Table 1
Carbon fiber properties.

Material	E_{1f} (GPa)	E_{2f} (GPa)	G_{12f} (GPa)	ν_{12f}	ν_{23f}	α_{1f} (1/K)	α_{2f} (1/K)
IM7 12K Carbon Fiber	276	23.1	27.6	0.35	0.30	−4.0E−7	6.0E−6

Table 2
Comparison of the effective tow properties at different temperatures.

Material Combination	E_{1t} (GPa)	E_{2t} (GPa)	G_{12t} (GPa)	ν_{12t}	ν_{23t}	α_{1t} (1/K)	α_{2t} (1/K)
IM7 fibers + RTM6 epoxy (see Table 2 in [17]) Used in simulations	221.38	13.18	7.17	0.35	0.35	−2.29E−7	2.23E−5
IM7 fibers + RTM6 epoxy at $T = 25°C$ (see Eqs. (6) and (7))	221.47	14.04	7.99	0.35	0.35	−2.40E−7	1.90E−5
IM7 fibers + RTM6 epoxy at $T = 100°C$ (see Eqs. (6) and (7))	221.38	13.22	7.21	0.35	0.35	−2.40E−7	2.11E−5
IM7 fibers + RTM6 epoxy at $T = 165°C$ (see Eqs. (6) and (7))	221.31	12.39	6.48	0.35	0.35	−2.45E−7	2.30E−5

the corresponding Poisson's ratios. In this particular composite material, due to tow crimp, the contraction along the z-axis (through-thickness direction) causes straightening of the warp and weft tows. As a result, the expected in-plane contraction due to Poisson's effect is partially compensated by the straightening of the weft tows.

5.2. Predictions of residual stresses

Numerical simulations of cooling after curing of the composite were performed to predict development of the residual stresses during manufacturing. It was assumed that the material is fully cured and free of stress in the beginning of the simulation. The UC was assigned a uniform initial temperature distribution of $T_0 = 165°C$, and then cooled from curing to room temperature by prescribing a uniform temperature drop of $\Delta T = -140°C$ in 40 increments. The temperature dependence of the Young's modulus and the CTE of the matrix was implemented using expressions 6 and 7.

Fig. 6a and b illustrate distributions of hydrostatic stress σ_H and von Mises stress σ_{VM} in the matrix at the final step of the simulation ($T = 25°C$). As expected, the intensity of hydrostatic stress is considerably higher than von Mises in the matrix pockets where the microcracking of the actual specimens was observed. Post-processing of the results shows that 6.0% of the matrix volume experiences residual stresses with the triaxility factor (defined as $\frac{\sigma_H}{\sigma_{VM}}$) higher than 2.

Figs. 7–9 present distributions of equivalent stresses in several representative locations within the unit cell. The equivalent stresses corresponding to the four stress-based failure criteria discussed in Section 3 are: $\sigma_{VM} = \sqrt{0.5[(\sigma_1-\sigma_2)^2 + (\sigma_1-\sigma_3)^2 + (\sigma_2-\sigma_3)^2]}$, $\sigma_H = \frac{1}{3}(\sigma_1 + \sigma_2 + \sigma_3)$, $\sigma_{parabolic} = \sigma_{VM}^2 + A\sigma_H$, $\sigma_{Bauwens} = \sigma_{VM} + C\sigma_H$. The locations of the considered cross-sections are indicated in the panels (a) of the figures. The colormap is chosen so that the black color corresponds to the values of equivalent stress in the matrix exceeding the limit for the corresponding criterion, see Section 3 for numerical values. Panel (b) in each figure shows the image of the cross-section obtained using X-ray computed microtomography (μCT). Black regions in the μCT images are cracks and voids that form during cooling after curing.

Fig. 7 shows distributions of the equivalent stresses in the slice made through the middle of the binder tow perpendicular to the weft direction. It can be seen that von Mises stress criterion (the corresponding distribution is given in panel (c)) predicts damage on the convex surfaces of the binder while the actual composite contains microcracks on the concave sides. It is evident that Bauwens criterion (panel (d)) significantly overpredicts the extent of damage predicting the entire resin volume to be above the critical value. Both parabolic (panel (e) and (f)) and dilatational energy (panel (g)) criteria appear to correctly predict the locations of the damaged regions within the unit cell. It is difficult to make an exact quantitative evaluation – it seems that the actual damaged area is larger than what is predicted by the parabolic criterion with the coefficients based on [23], but smaller than what is predicted by the parabolic criterion with the coefficients based on [15] and the dilatational energy criterion. Note that propagation of damage is not included in the presented numerical models. Cracks when formed would alleviate the stress concentrations and limit the extent of further damage to surrounding matrix. Thus, it is expected that the numerically predicted damaged areas are larger than the microcracked regions in the actual specimens. So it appears that the parabolic criterion with the coefficients based on [15] and the dilatational energy criterion correlate with the microtomography data better.

Analysis of the slice perpendicular to the warp direction as presented in Fig. 8 shows similar trends. Von Mises criterion (panel (c)) fails to predict damage at the interface between the warp and the binder tows. Bauwens criterion (panel (d)) predicts complete failure of the matrix in the cross-section. In this slice, the parabolic criterion with the coefficients based on [23] (panel (e)) underpredicts the actual damage. When comparing the parabolic criterion with the coefficients based on [15] (panel (f)) and dilatational energy criterion (panel (g)), the latter appears closer to the μCT observations (panel (b)), however, as discussed in the previous paragraph some overprediction by the numerical simulations is expected. Therefore, both may provide useful predictions.

An example of a cross-section without considerable damage is presented in Fig. 9. The only identifiable defect in the μCT slice (inside the white circle in panel (b)) looks like a trapped gas bubble. When comparing predictions of different failure criteria, we observe that von Mises criterion, parabolic criterion with coefficients based on [23] and the dilatational energy criterion do not predict any damage within this slice. As in the previous slices, Bauwens criterion predicts failure of the entire matrix within the cross-section. Parabolic criterion with coefficients based on [15] predicts more damage in the matrix than observed in the μCT image.

Based on our comparisons of the criteria, it appears that the dilatational energy criterion and the parabolic criterion with coefficients

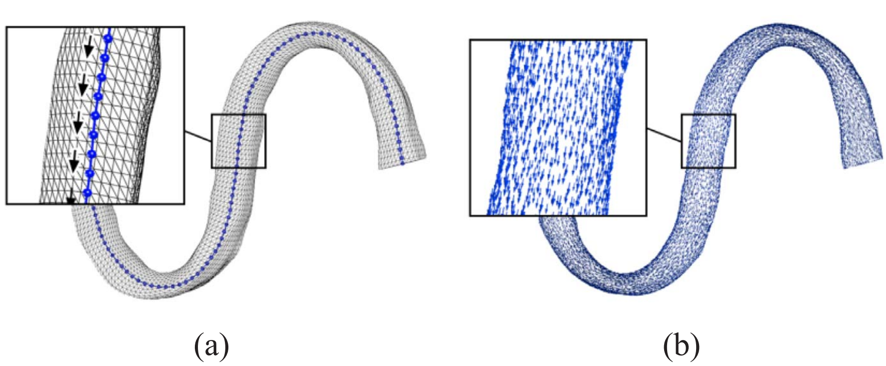

Fig. 5. Assignment of the material orientations for a tow: (a) center points connected into a polyline, (b) first principal material orientation after mapping of the polyline onto tow FE mesh.

Table 3
Effective elastic properties of the unit cell.

$E_{x\ (warp)}$, (GPa)	$E_{y\ (weft)}$, (GPa)	$E_{z\ (binder)}$, (GPa)	ν_{xy}	ν_{yz}	ν_{xz}	G_{xy}, (GPa)	G_{yz}, (GPa)	G_{zx}, (GPa)
57.4	67.7	11.7	0.0472	0.403	0.417	4.36	2.97	3.10

based on [15] are more appropriate for predictions of processed-induced matrix damage in 3D woven composites due to mismatch in the coefficients of thermal expansion between the matrix and the reinforcement than other criteria discussed in this paper. This observation is also supported by analyses of other cross-sections not presented in this paper.

We attribute the differences in predictive power of the parabolic criterion with two different sets of material constants (based on [15] and [23]) to different types of mechanical experiments used to evaluate the parameters A and B^{crit}. It is also worth noting that the consistent overprediction of damage by the Bauwens criterion could be caused by the inappropriate choice of the material parameters based on the limited set of data (tension and compression only).

6. Conclusions

Meso-scale finite element simulations were performed to predict initiation of processing-induced damage in 3D woven composites due to mismatch in the thermal expansion coefficients between fibers and matrix. Carbon fiber/epoxy resin composite with high level of through-thickness reinforcement (one-to-one orthogonal architecture) was considered because such reinforcement architectures have been shown to develop processing-induced microcracks. Combination of digital fabric mechanics simulations [27,34,35], geometry processing and finite element meshing technique [29] was used to generate highly realistic FEA model of the composite's periodic unit cell.

A complete distribution of the residual stresses within the composite unit cell was obtained from FEA. It was observed that a significant amount of matrix material in resin rich areas was subjected to high levels of hydrostatic tension. Analysis of the numerical results showed that 6.0% of the intertow matrix experienced residual stresses with the triaxility factor higher than 2.

The applicability of four commonly used failure criteria for prediction of processing-induced damage in the matrix of the 3D woven composite was investigated. The critical value for the von Mises stress was chosen from the experimental studies of the RTM6 resin reported in [17]. The critical value of the dilatational energy was taken from [23]. Two sets of material parameters were utilized for the parabolic stress criterion: constants obtained from tension and compression tests of [23] and uniaxial tension and torsion tests of [15]. Finally, the parameters for the Bauwens criterion were based on tension and compression results of [23].

The considered criteria predict considerably different critical hydrostatic stress values in the absence of the deviatoric stresses and critical von-Mises stress values in the absence of the hydrostatic stresses. The disparity can be explained by the fact that the experiments used to calculate the parameters in these criteria activated different material failure modes. These observations indicate that choosing the failure criterion at a given point based on the local state of stress may provide more accurate predictions than using the same criterion for the entire volume of the material.

Comparison of the numerical damage predictions with X-ray computed microtomography data indicates that the dilatational energy density criterion and the parabolic stress criterion appear to be the most suitable for analysis of residual stresses leading to microcracking due to mismatch of CTEs during cooling after curing. However, the accuracy of the latter criterion depends on the choice of experiments used to determine the material parameters A and B^{crit}. One can speculate that better predictions of failure with parabolic criterion are achieved when the experiments used to determine these parameters activate relevant failure mechanisms in the material.

Our observations indicate that the FEA model presented in this paper can be successfully utilized to predict susceptibility of 3D woven composites to processing-induced microcracking. It has the potential of lowering the development costs of new 3D woven architectures by reducing the need for manufacturing of expensive physical prototypes required for studying the microcracking phenomenon.

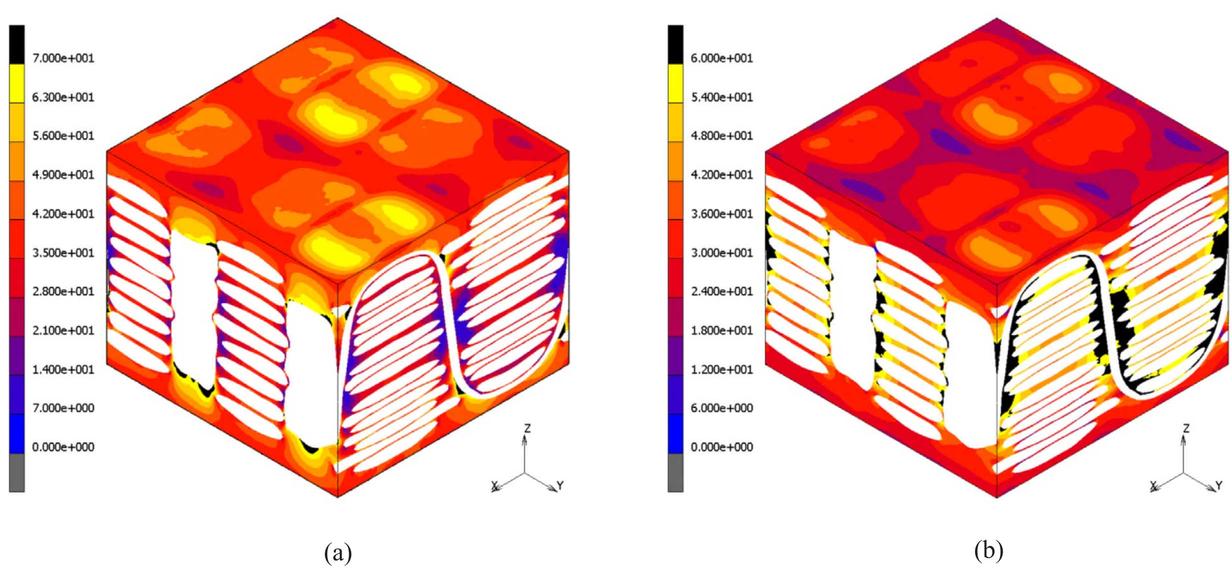

Fig. 6. (a) Von Mises stress distribution; (b) hydrostatic stress distribution (tows are not shown).

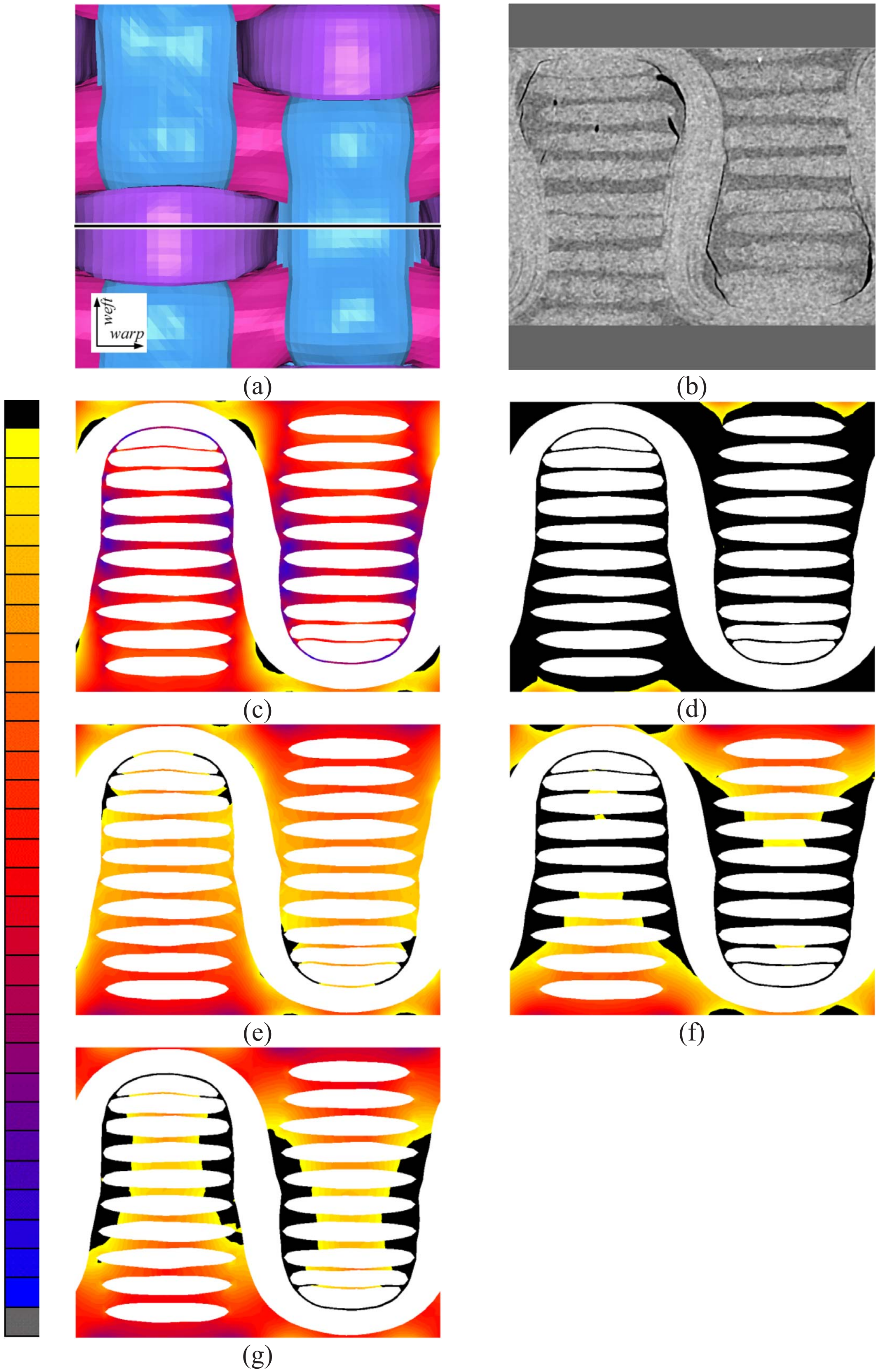

Fig. 7. Distribution of the equivalent stresses in the matrix of the UC after cooling: (a) slice location within the UC; (b) microtomography image; (c) von Mises; (d) Bauwens; (e) parabolic criterion with coefficients based on [23]; (f) parabolic criterion with coefficients based on [15]; (g) dilatational energy criterion. The colormap ranges from blue (zero) to yellow with regions above critical value shown in black. (For interpretation of the references to color in this figure legend, the reader is referred to the web version of this article.)

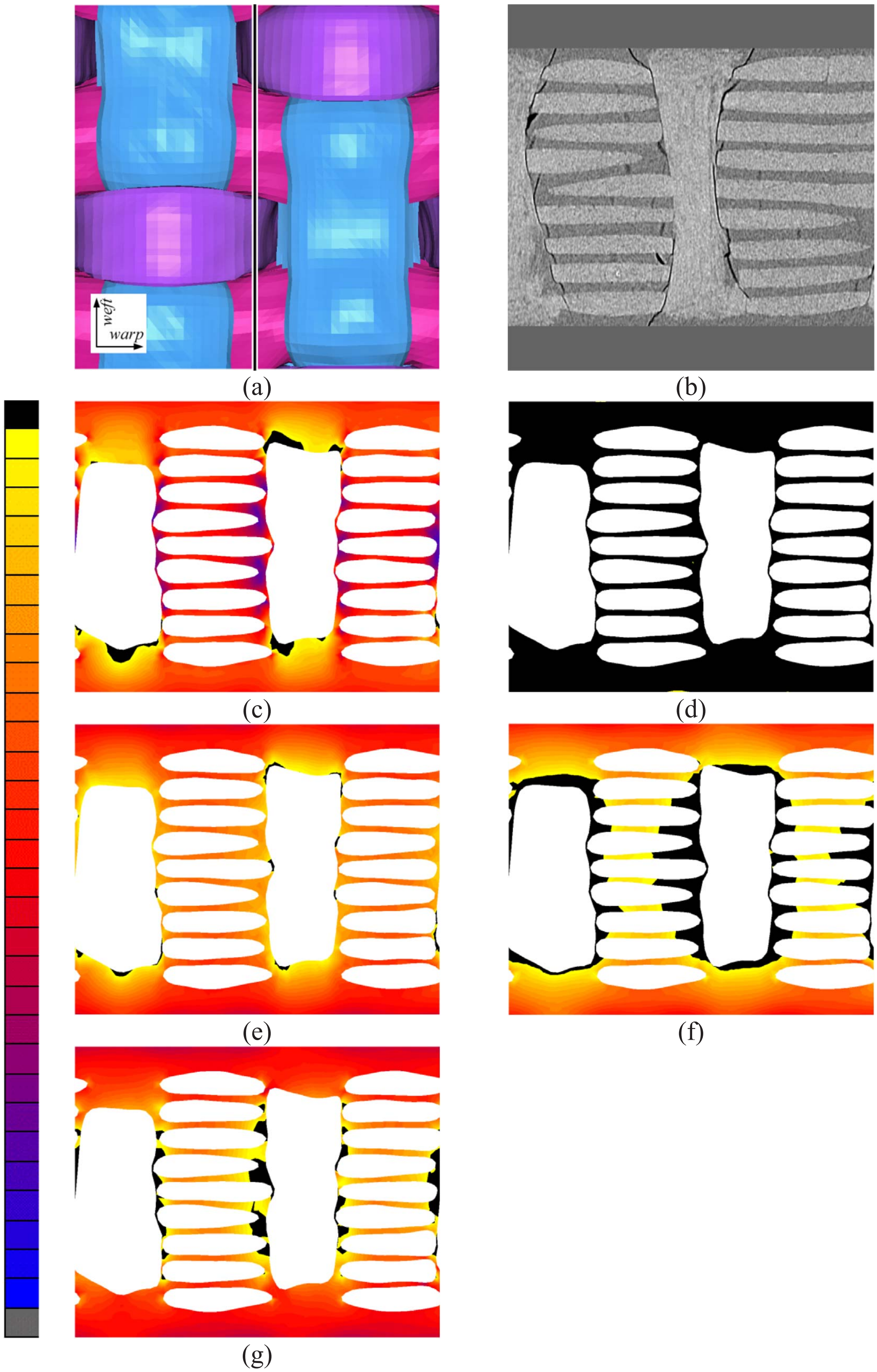

Fig. 8. Distribution of the equivalent stresses in the matrix of the UC after cooling: (a) slice location within the UC; (b) microtomography image; (c) von Mises; (d) Bauwens; (e) parabolic criterion with coefficients based on [23]; (f) parabolic criterion with coefficients based on [15]; (g) dilatational energy criterion. The colormap ranges from blue (zero) to yellow with regions above critical value shown in black. (For interpretation of the references to color in this figure legend, the reader is referred to the web version of this article.)

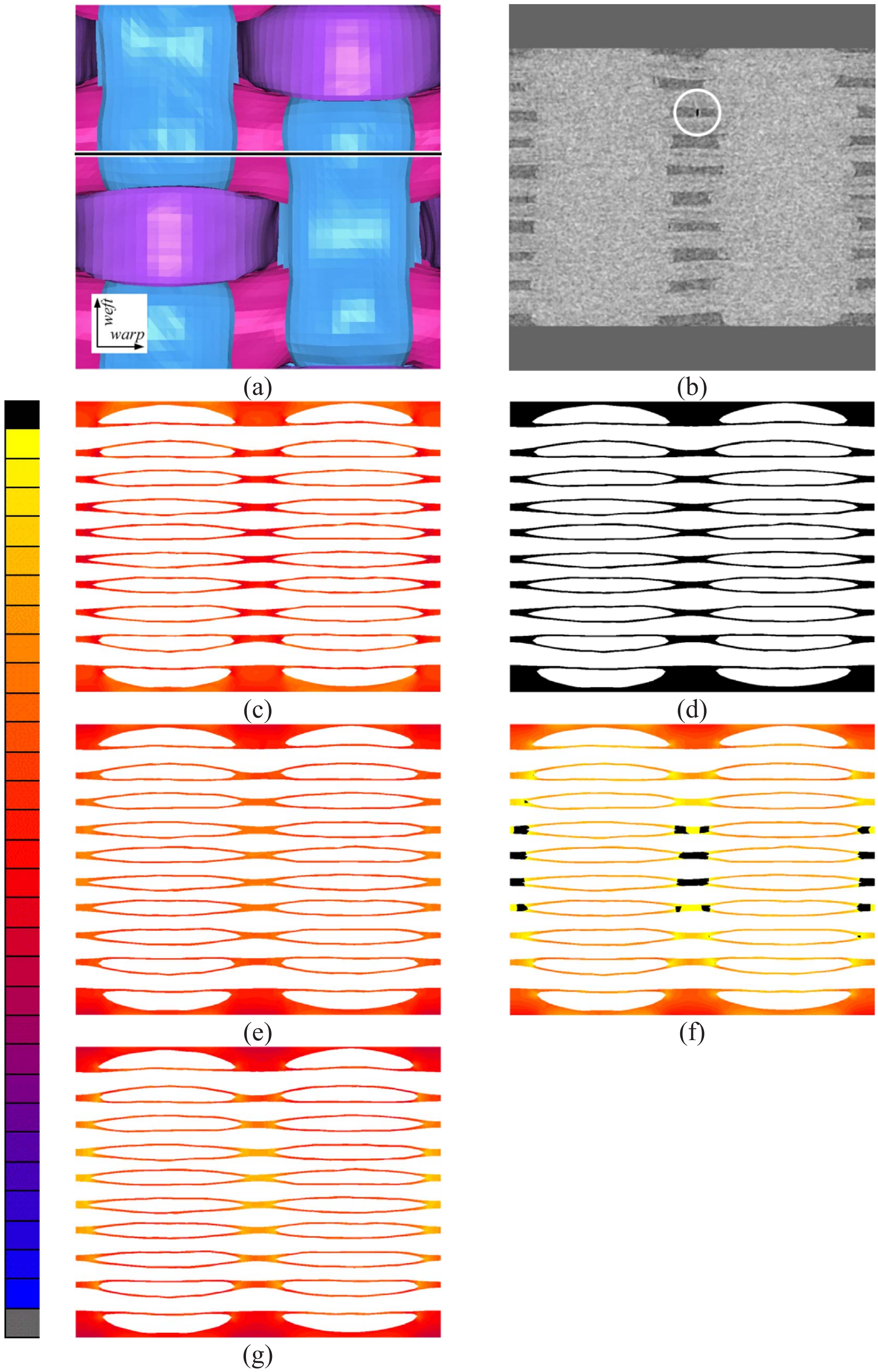

Fig. 9. Distribution of the equivalent stresses in the matrix of the UC after cooling: (a) slice location within the UC; (b) microtomography image with a microvoid highlighted by a white circle; (c) von Mises; (d) Bauwens; (e) parabolic criterion with coefficients based on [23]; (f) parabolic criterion with coefficients based on [15]; (g) dilatational energy criterion. The colormap ranges from blue (zero) to yellow with regions above critical value shown in black. (For interpretation of the references to color in this figure legend, the reader is referred to the web version of this article.)

Acknowledgements

This material is based upon work supported by the National Science Foundation under Grant No. CMMI-1100409. This research was performed in collaboration with Albany Engineered Composites (AEC), Inc. and was also supported by the New Hampshire Innovation Research Center. We are grateful to Harun Bayraktar and Jon Goering (AEC) for providing the X-ray computed microtomography images of the composites with processing-induced damage and for helpful discussion of the mechanics of 3D woven composites. Financial support from the New Mexico Space Grant Consortium through NASA Cooperative Agreement NNX15AK41A is also gratefully acknowledged.

References

[1] Tong L, Mouritz AP, Bannister MK. 3D fibre reinforced polymer composites. Elsevier; 2002.
[2] Heinrich C, Aldridge M, Wineman AS, Kieffer J, Waas AM, Shahwan KW. The role of curing stresses in subsequent response, damage and failure of textile polymer composites. J Mech Phys Solids 2013;61:1241–64. http://dx.doi.org/10.1016/j.jmps.2012.12.005.
[3] Guevara-Morales A, Figueroa-López U. Residual stresses in injection molded products. J Mater Sci 2014;49:4399–415. http://dx.doi.org/10.1007/s10853-014-8170-y.
[4] Jin KK, Oh JH, Ha SK. Effect of fiber arrangement on residual thermal stress distributions in a unidirectional composite. J Compos Mater 2006;41:591–611. http://dx.doi.org/10.1177/0021998306065290.
[5] Zhao LG, Warrior NA, Long AC. A micromechanical study of residual stress and its effect on transverse failure in polymer–matrix composites. Int J Solids Struct 2006;43:5449–67. http://dx.doi.org/10.1016/j.ijsolstr.2005.08.012.
[6] Yang L, Yan Y, Ma J, Liu B. Effects of inter-fiber spacing and thermal residual stress on transverse failure of fiber-reinforced polymer–matrix composites. Comput Mater Sci 2013;68:255–62. http://dx.doi.org/10.1016/j.commatsci.2012.09.027.
[7] Lu C, Chen P, Yu Q, Gao J, Yu B. Thermal residual stress distribution in carbon fiber/novel thermal plastic composite. Appl Compos Mater 2008;15:157–69. http://dx.doi.org/10.1007/s10443-008-9064-4.
[8] Han G, Guan Z, Li Z, Zhang M, Bian T, Du S. Multi-scale modeling and damage analysis of composite with thermal residual stress. Appl Compos Mater 2015;22:289–305. http://dx.doi.org/10.1007/s10443-014-9407-2.
[9] Karami G, Grundman N, Abolfathi N, Naik A. Thermoelastic characterization and evaluation of residual stresses in bi-directional fibrous composites. Appl Compos Mater 2008;15:259–72. http://dx.doi.org/10.1007/s10443-008-9071-5.
[10] Han G, Guan Z, Du S. Damage evolution and multi-scale analysis of carbon fiber-reinforced cross-ply laminate with thermal residual stress. Compos Interfaces 2015;22:331–42. http://dx.doi.org/10.1080/09276440.2015.1029799.
[11] Sweeting RD, Thomson RS. The effect of thermal mismatch on Z-pinned laminated composite structures. Compos Struct 2004;66:189–95. http://dx.doi.org/10.1016/j.compstruct.2004.04.037.
[12] Xiong JJ, Shenoi RA, Gao J. An analytical model to predict residual thermal stress in 2D orthogonal plain weave fabric composites. Int J Solids Struct 2009;46:1872–83. http://dx.doi.org/10.1016/j.ijsolstr.2008.12.026.
[13] Hirsekorn M, Grail G, Poitrimolt M, Agogue R, Beauchene P. Multi-scale and multi-physics coupled modeling of the evolution of internal stresses and part shape of carbon-epoxy composites. In: Proceedings of the 15th European Conference on Composite Materials ECCM15, Venice, Italy: 2012, p. 24–8.
[14] Fiedler B, Hojo M, Ochiai S. The influence of thermal residual stresses on the transverse strength of CFRP using FEM. Composites Part A 2002;33:1323–6. http://dx.doi.org/10.1016/S1359-835X(02)00169-0.
[15] Hobbiebrunken T, Hojo M, Fiedler B, Tanaka M, Ochiai S, Schulte K. Thermomechanical analysis of micromechanical formation of residual stresses and initial matrix failure in CFRP. JSME Int J Ser, A 2004;47:349–56. http://dx.doi.org/10.1299/jsmea.47.349.
[16] Hobbiebrunken T, Fiedler B, Hojo M, Ochiai S, Schulte K. Microscopic yielding of CF/epoxy composites and the effect on the formation of thermal residual stresses. Compos Sci Technol 2005;65:1626–35. http://dx.doi.org/10.1016/j.compscitech.2005.02.003.
[17] Brauner C, Block T, Purol H, Herrmann A. Microlevel manufacturing process simulation of carbon fiber/epoxy composites to analyze the effect of chemical and thermal induced residual stresses. J Compos Mater 2012;46:2123–43. http://dx.doi.org/10.1177/0021998311430157.
[18] Svanberg JM, Holmberg JA. Prediction of shape distortions Part I. FE-implementation of a path dependent constitutive model. Composites Part A 2004;35:711–21. http://dx.doi.org/10.1016/j.compositesa.2004.02.005.
[19] Ding A, Li S, Wang J, Ni A. A new analytical solution for spring-in of curved composite parts. Compos Sci Technol 2017;142:30–40. http://dx.doi.org/10.1016/j.compscitech.2017.01.024.
[20] Ding A, Li S, Wang J, Ni A, Zu L. A new path-dependent constitutive model predicting cure-induced distortions in composite structures. Composites Part A 2017;95:183–96. http://dx.doi.org/10.1016/j.compositesa.2016.11.032.
[21] Magniez K, Vijayan A, Finn N. Apparent volumetric shrinkage study of RTM6 resin during the curing process and its effect on the residual stresses in a composite. Polym Eng Sci 2012;52:346–51. http://dx.doi.org/10.1002/pen.22088.
[22] Gross TS, Jafari H, Kusch J, Tsukrov I, Drach B, Bayraktar H, et al. Measuring failure stress of RTM6 epoxy resin under purely hydrostatic tensile stress using constrained tube method. Exp Tech 2017;41:45–50. http://dx.doi.org/10.1007/s40799-016-0153-2.
[23] Asp LE, Marklund E, Varna J, Olsson R. Multiscale modeling of non-crimp fabric composites. In: Proceedings of the 2012 International Mechanical Engineering Congress & Exposition (IMECE2012), Houston, TX: 2012, p. 1–10.
[24] Lomov S, Perie G, Ivanov D, Verpoest I, Marsal D. Modeling three-dimensional fabrics and three-dimensional reinforced composites: challenges and solutions. Text Res J 2011;81:28–41. http://dx.doi.org/10.1177/0040517510385169.
[25] Fagiano C, Genet M, Baranger E, Ladevèze P. Computational geometrical and mechanical modeling of woven ceramic composites at the mesoscale. Compos Struct 2014;112:146–56. http://dx.doi.org/10.1016/j.compstruct.2014.01.045.
[26] Joglekar S, Pankow M. Modeling of 3D woven composites with realistic geometry for accurate prediction of kinking under compressive loads. In: Proceedings of the American Society for Composites – 30th Technical Conference, ACS 2015; 2015. doi:10.1016/j.compstruct.2016.10.070.
[27] Wang Y, Sun X. Digital-element simulation of textile processes. Compos Sci Technol 2001;61:311–9. http://dx.doi.org/10.1016/S0266-3538(00)00223-2.
[28] Wang Y, Miao Y, Swenson D, Cheeseman BA, Yen C-F, LaMattina B. Digital element approach for simulating impact and penetration of textiles. Int J Impact Eng 2010;37:552–60. http://dx.doi.org/10.1016/j.ijimpeng.2009.10.009.
[29] Drach A, Drach B, Tsukrov I. Processing of fiber architecture data for finite element modeling of 3D woven composites. Adv Eng Softw 2014;72:18–27. http://dx.doi.org/10.1016/j.advengsoft.2013.06.006.
[30] Verpoest I, Lomov S. Virtual textile composites software WiseTex: integration with micro-mechanical, permeability and structural analysis. Compos Sci Technol 2005;65:2563–74. http://dx.doi.org/10.1016/j.compscitech.2005.05.031.
[31] Mahadik Y, Hallett SR. Finite element modelling of tow geometry in 3D woven fabrics. Composites Part A 2010;41:1192–200. http://dx.doi.org/10.1016/j.compositesa.2010.05.001.
[32] Lin H, Brown LP, Long AC. Modelling and simulating textile structures using TexGen. Adv Mater Res 2011;331:44–7. http://dx.doi.org/10.4028/www.scientific.net/AMR.331.44.
[33] Green SD, Long AC, El Said BSF, Hallett SR. Numerical modelling of 3D woven preform deformations. Compos Struct 2014;108:747–56. http://dx.doi.org/10.1016/j.compstruct.2013.10.015.
[34] Zhou G, Sun X, Wang Y. Multi-chain digital element analysis in textile mechanics. Compos Sci Technol 2004;64:239–44. http://dx.doi.org/10.1016/S0266-3538(03)00258-6.
[35] Miao Y, Zhou E, Wang Y, Cheeseman B. Mechanics of textile composites: micro-geometry. Compos Sci Technol 2008;68:1671–8. http://dx.doi.org/10.1016/j.compscitech.2008.02.018.
[36] Sherburn M. Geometric and mechanical modelling of textiles. University of Nottingham; 2007.
[37] Lomov S, Ivanov D, Verpoest I, Zako M, Kurashiki T, Nakai H, et al. Meso-FE modelling of textile composites: road map, data flow and algorithms. Compos Sci Technol 2007;67:1870–91. http://dx.doi.org/10.1016/j.compscitech.2006.10.017.
[38] Rinaldi RG, Blacklock M, Bale H, Begley MR, Cox BN. Generating virtual textile composite specimens using statistical data from micro-computed tomography: 3D tow representations. J Mech Phys Solids 2012;60:1561–81. http://dx.doi.org/10.1016/j.jmps.2012.02.008.
[39] Drach B, Drach A, Tsukrov I, Penverne M, Lapusta Y. Finite Element Models of 3D Woven Composites Based on Numerically Generated Micro-Geometry of Reinforcement. In: Proceedings of the American Society for Composites 2014–29th Technical Conference on Composite Materials, San Diego, CA; 2014.
[40] Asp LE, Berglund LA, Talreja R. A criterion for crack initiation in glassy polymers subjected to a composite-like stress state. Compos Sci Technol 1996;56:1291–301. http://dx.doi.org/10.1016/S0266-3538(96)00090-5.
[41] Kim JW, Medvedev GA, Caruthers JM. Observation of yield in triaxial deformation of glassy polymers. Polymer (United Kingdom) 2013;54:2821–33. http://dx.doi.org/10.1016/j.polymer.2013.03.042.
[42] Tsukrov I, Drach A, Drach B, Bayraktar H, Goering J, Gross TS. Numerical Predictions of Damage Initiation in 3D Woven Composites under Various Loading Conditions. In: Proceedings of the American Society for Composites 2014–29th Technical Conference on Composite Materials, San Diego, CA; 2014.
[43] Mclendon WR, Whitcomb JD. Failure Initiation Prediction in Textile Composites Under Complex Thermo-Mechanical Loading Based on Meso-scale Analysis. In: 53rd AIAA/ASME/ASCE/AHS/ASC Structures, Structural Dynamics and Materials Conference; 2012. p. 1–18.
[44] Koumpias AS, Tserpes KI, Pantelakis S. Progressive damage modelling of 3D fully interlaced woven composite materials. Fatigue Fract Eng Mater Struct 2014;37:696–706. http://dx.doi.org/10.1111/ffe.12142.
[45] Courtney TH. Mechanical behavior of materials. Second ed. Chicago: Waveland Press, Inc.; 2005.
[46] Gent AN, Lindley PB. Internal rupture of bonded rubber cylinders in tension. Proc R Soc London, Ser A 1959;249:195–205. http://dx.doi.org/10.1098/rspa.1959.0016.
[47] Asp LE, Berglund L, Gudmundson P. Effects of a composite-like stress state on the fracture of epoxies. Compos Sci Technol 1995;53:27–37. http://dx.doi.org/10.1016/0266-3538(94)00075-1.
[48] Plepys A, Vratsanos MS, Farris RJ. Determination of residual stresses using incremental linear elasticity. Compos Struct 1994;27:51–6. http://dx.doi.org/10.1016/0263-8223(94)90066-3.
[49] Christensen RM. A comprehensive theory of yielding and failure for isotropic materials. J Eng Mater Technol 2007;129:173. http://dx.doi.org/10.1115/1.2712847.

[50] Chamis C. Mechanics of composite materials: past, present, and future. J Compos Tech Res 1989;11:3–14. http://dx.doi.org/10.1520/CTR10143J.
[51] Hashin Z, Shtrikman S. A variational approach to the theory of the elastic behaviour of multiphase materials. J Mech Phys Solids 1963;11:127–40. http://dx.doi.org/10.1016/0022-5096(63)90060-7.
[52] Tsukrov I, Bayraktar H, Giovinazzo M, Goering J, Gross TS, Fruscello M, et al. Finite element modeling to predict cure-induced microcracking in three-dimensional woven composites. Int J Fract 2011;172:209–16. http://dx.doi.org/10.1007/s10704-011-9659-x.
[53] Tsukrov I, Drach B, Gross TS. Effective stiffness and thermal expansion coefficients of unidirectional composites with fibers surrounded by cylindrically orthotropic matrix layers. Int J Eng Sci 2012;58:129–43. http://dx.doi.org/10.1016/j.ijengsci.2012.03.032.
[54] Schapery RA. Thermal expansion coefficients of composite materials based on energy principles. J Compos Mater 1968;2:380–404. http://dx.doi.org/10.1177/002199836800200308.
[55] Hashin Z. Analysis of properties of fiber composites with anisotropic constituents. J Appl Mech 1979;46:543–50.
[56] Tsukrov I, Giovinazzo M, Vyshenska K, Bayraktar H, Goering J, Gross TS. Comparison of two approaches to model cure-induced microcracking in three-dimensional woven composites. In: Proceedings of the 2012 International Mechanical Engineering Congress & Exposition (IMECE2012), Houston, TX; 2012, p. 1–6.
[57] Li S. General unit cells for micromechanical analyses of unidirectional composites. Composites Part A 2001;32:815–26. http://dx.doi.org/10.1016/S1359-835X(00)00182-2.
[58] Segurado J, Llorca J. A numerical approximation to the elastic properties of sphere-reinforced composites. J Mech Phys Solids 2002;50:2107–21. http://dx.doi.org/10.1016/S0022-5096(02)00021-2.
[59] Drach B, Tsukrov I, Trofimov A. Comparison of full field and single pore approaches to homogenization of linearly elastic materials with pores of regular and irregular shapes. Int J Solids Struct 2016. http://dx.doi.org/10.1016/j.ijsolstr.2016.06.023.
[60] Xia Z, Zhang Y, Ellyin F. A unified periodical boundary conditions for representative volume elements of composites and applications. Int J Solids Struct 2003;40:1907–21. http://dx.doi.org/10.1016/S0020-7683(03)00024-6.
[61] Software MSC. MSC Marc 2016 Volume A: theory and User. Information 2016.
[62] Vyshenska K. Thesis: numerical and experimental studies of mechanical behavior and cure induced stresses in 3D carbon/epoxy composites. University of New Hampshire; 2014.